Three-dimensional numerical models of the evolution of pull-apart basins

A.G. Petrunin, S.V. Sobolev

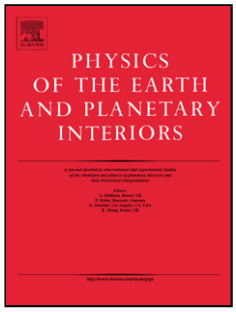

Title: Three-dimensional numerical models of the evolution of pull-apart basins

Authors: A.G. Petrunin, S.V. Sobolev

PII: S0031-9201(08)00236-7
DOI: doi:10.1016/j.pepi.2008.08.017
Reference: PEPI 5055

To appear in: *Physics of the Earth and Planetary Interiors*

Received date: 30-11-2007
Revised date: 5-8-2008
Accepted date: 17-8-2008

Please cite this article as: Petrunin, A.G., Sobolev, S.V., Three-dimensional numerical models of the evolution of pull-apart basins, *Physics of the Earth and Planetary Interiors* (2007), doi:10.1016/j.pepi.2008.08.017

Three-dimensional numerical models of the evolution of pull-apart basins

A.G. Petrunin* and S.V. Sobolev

GeoForschungsZentrum, Telegrafenberg, D-14473 Potsdam, Germany

Schmidt Institute of Physics of the Earth, B. Gruzinskaya 10, 123995 Moscow, Russia

* - corresponding author

Abstract

Pull-apart basins are depressions that form as the result of crustal extension along strike-slip systems where the sense of fault stepping or bending coincides with that of fault slip. They are common features of strike-slip systems. We perform a number of numerical thermomechanical experiments to explore how the rheology of the lithosphere influences basin evolution and lithospheric structure beneath the basin. Our modeling shows that basin subsidence results from the competition of extension of the brittle part of the lithosphere, which leads to its subsidence, and of the compensating flow of the deeper ductile part of the lithosphere, which pushes the extended brittle block upwards. The result of this competition is the subsidence rate. Strain partitioning beneath the basin and crustal structures is controlled by (i) the thickness of the brittle layer and basin width, (ii) the magnitude of strike-slip displacement, (iii) the rate of frictional softening of the crust, and (iv) the viscosity of the ductile part of the lithosphere. The thickness of the brittle layer and the viscosity of the underlying ductile part of the lithosphere in turn depend on temperature, composition and material softening. We interpret the modeling results, deducing simple analytical expressions based on the "brittle brick stretching" (BBS) approach, which despite its simplicity describes the structure and evolution of pull-apart basins reasonably well. We also demonstrate that the structure and evolution of the Dead Sea Basin, located at a left step of the Dead Sea Transform in the Middle East, is consistent with a BBS type of deformation with only a minor contribution from compensational flow in the ductile part of the lithosphere. Finally, we show that the formation of a deep narrow pull-apart basin in relatively cold lithosphere, as in the

Dead Sea Basin, requires very low friction at major faults (lower than 0.1-0.2). If this condition is not satisfied, strike-slip deformation does not localise and deep basins do not form.

Keywords: Pull-apart basin; transform fault; thermomechanical modeling; tectonophysics

1 Introduction

By definition, a pull-apart basin is a depression formed as a result of crustal extension along a strike-slip system where the sense of fault stepping or bending coincides with the sense of fault motion. Pull-apart structures are common along continental transform faults, and are found along both intra- and interplate strike-slip zones (Burchfiel and Stewart, 1966; Christie-Blick and Biddle, 1985; Sylvester, 1988). Several mechanisms have been proposed for their formation, the most popular of which is local extension between two en echelon strike-slip fault segments (e.g., Crowel, 1974; Garfunkel, 1981; Aydin and Nur, 1985; Twiss and Moores, 1992). Local extension is accommodated in the brittle domain of the lithosphere, where the main transform fault steps or bends, forming a deep sedimentary basin (e.g., Christie-Blick and Biddle, 1985, Petrunin and Sobolev, 2006). The internal structures of these basins are highly variable in both space and time due to the complex stress distribution and heterogeneous crustal rheology around the terminations of the delimiting faults. This complexity has led to several unresolved problems regarding the kinematics and dynamics of pull-apart basins (e.g., Rodgers, 1980; Garfunkel, 1981; Ben Avraham and Zoback, 1992; Katzman et al., 1995; ten Brink et al., 1996). Moreover, there is only rare documentation of time-dependent deformation patterns

within pull-apart basins and how they are related to the adjacent deformed structural domains.

Geophysical and geological observations provide important information about the recent structures of pull-apart basins and the character of their recent tectonic deformation. Using the observed data as constraints, analog or numerical mechanical modeling can give some useful insights that are beyond direct observation, e.g., probable scenarios of initiation and temporal evolution of the basins, deformation patterns during evolution, possible temperature regime and rheology. However, the mechanical modeling of pull-apart basins is complicated because of their 3-D nature. This is why analog modeling is most popular (Richard et al., 1995; McClay and Dooley, 1995; Rahe et al., 1998; McClay and Bonora, 2001; Calvez and Vendeville, 2002; Atmaoui et al., 2006). Such modeling focuses mostly on simulating pull-apart structure initiation in certain geotectonic settings (e.g., Smit, 2005; Atmaoui et al., 2006) and understanding the nature of near-surface strain distribution during basin evolution. Although the analog modeling is three-dimensional and deals with large strain, it has a strong disadvantage as it cannot operate with realistic temperature-dependant visco-elasto-plastic rheologies and it does not couple thermal and mechanical processes.

The other way to simulate pull-apart basin evolution and structure is using mechanical or thermo-mechanical numerical modeling. So far, this kind of modeling has been limited to either 2-D thin-plate approximations, which do not resolve the depth distribution of stress and strain (e.g., Segall and Pollard, 1980) or to 3-D models in the small-strain elastic approximation (Katzman et al., 1995; ten Brink et al., 1996),

which strongly oversimplify real rheology (which is visco-elastic-plastic), and therefore can only investigate geodynamic tendencies rather than long-term evolution.

There is therefore a clear necessity to model the long-term evolution of pull-apart basins incorporating coupled thermal and mechanical processes and a realistic rheology. Petrunin and Sobolev (2006) analyzed some factors that control the structure and evolution of pull-apart basins using models with a realistic temperature- and stress-dependent visco-elasto-plastic rheology and allowing for large strains. However, that study did not consider a number of important factors, like the effect of friction at major faults on the evolution of the basin, or the influence of the model resolution. Here, we use the same modeling technique as Petrunin and Sobolev (2006) to study the evolution of a pull-apart basin in more detail. In particular, compared to that paper, here we compute models with higher resolution and within larger model domains, which significantly reduces the influence of boundary conditions and allows us to simulate pull-apart structures even in a rather cold lithosphere. We also consider the influence of the plastic softening rate (Lavier et al., 2000; Huismans and Beaumont, 2002; Babeyko et al., 2002) and the friction coefficient at major faults. We propose a generalized interpretation of the numerical experiments and provide analytical relations for asymptotic cases. Finally, we discuss the application of our models for the Dead Sea pull-apart basin.

2. Modeling features

2.1 Modeling technique

In this study, we apply a numerical technique focused on the three-dimensional case when the structure and displacements fields allow us to define a special direction (x_3, Fig. 1) like the strike. The displacement field and structure in some cases may change more slowly in that direction than in the other two (x_1,x_2), although this is not obligatory.

We divide the model area into a series of two-dimensional parallel sections in the plane (x_1, x_2). At each section, we apply an extended two-dimensional finite-element numerical technique (Sobolev et al., 2005). All directional derivatives with respect to the coordinate x_3 are calculated using the standard second-order accurate finite-difference scheme. To determine the derivatives at the outermost sections, we assume that all parameters outside the modeling area remain unchanged in space along the x_3 axis and are equal to their values in the last sections.

In most of our models, the structure and displacement fields change more slowly in the x3 direction than in the other two. In these cases, the distance between the two-dimensional Lagrangian sections in our models is ten times larger than the finite element size within the sections. However, as a resolution test, in the Appendix we also present a model with spacing between the sections similar to the finite element size within them.

We model the deformation process by numerically integrating a fully-coupled system of three-dimensional conservation equations for momentum (Eq. 1), mass (Eq. 2) and energy (Eq. 3).

$$-\frac{\partial p}{\partial x_i}+\frac{\partial \tau_{ij}}{\partial x_j}+\rho g_i=0, \quad i=1,3 \tag{1}$$

$$\frac{1}{K}\frac{dp}{dt}-\alpha\frac{dT}{dt}=-\frac{\partial v_i}{\partial x_i}, \tag{2}$$

$$\rho C_p\frac{dT}{dt}=\frac{\partial}{\partial x_i}\left(\lambda(x_i,T)\frac{\partial T}{\partial x_i}\right)+\tau_{ij}\dot{\varepsilon}_{ij}+\rho A \tag{3}$$

Here, the Einstein summation convention applies and x_i are coordinates, t – time, v_i – velocities, p – pressure, τ_{ij} and $\dot{\varepsilon}_{ij}$ - stress and strain rate deviators, respectively, d/dt – convective time derivative, ρ – density, g_i – gravity vector, K – bulk modulus, α – coefficient of thermal expansion, T – temperature, C_p – heat capacity, λ – heat conductivity, and A – radiogenic heat productivity.

These equations are solved together with appropriate rheological relations that link the strain and stress rates. In our approach, we use a constitutive elasto-visco-plastic rheology. According to the additive decomposition rule, the overall deviatoric strain rate includes elastic, viscous and plastic components:

$$\dot{\varepsilon}_{ij}=\dot{\varepsilon}_{ij}^{(e)}+\dot{\varepsilon}_{ij}^{(v)}+\dot{\varepsilon}_{ij}^{(pl)}=\frac{1}{2G}\frac{\hat{d}\tau_{ij}}{dt}+\frac{\tau_{ij}}{2\eta_{eff}}+\dot{\varepsilon}_{ij}^{(pl)} \tag{4}$$

Here, G is the elastic shear modulus, $\hat{d}\tau_{ij}/dt$ – Jaumann co-rotational deviatoric stress rate, and η_{eff} is effective viscosity (Kameyama et al., 1999), including three competing creep mechanisms: diffusion, dislocation and Peierls creep. The

mechanism that produces the highest viscous strain rate becomes the dominant creep mechanism at a given temperature and stress:

$$\dot{\varepsilon}_{eff}^{(v)} = \dot{\varepsilon}_d + \dot{\varepsilon}_n + \dot{\varepsilon}_p \ , \tag{5}$$

where $\dot{\varepsilon}_d$ is diffusion creep:

$$\dot{\varepsilon}_d = B_d \tau_{II} \exp\left(-\frac{E_d + pV_a^d}{RT}\right), \tag{6}$$

$\dot{\varepsilon}_n$ is dislocation, power-law creep:

$$\dot{\varepsilon}_n = B_n \tau_{II}^n \exp\left(-\frac{E_n + pV_a^n}{RT}\right), \tag{7}$$

and $\dot{\varepsilon}_d$ is Peierls creep:

$$\dot{\varepsilon}_p = B_p \exp\left[-\frac{E_d + pV_a^p}{RT}\left(1-\frac{\tau_{II}}{\tau_p}\right)^q\right], \quad \tau_{II} \geq 200\,MPa\,. \tag{8}$$

The effective viscosity is then calculated as:

$$\eta_{eff} = \frac{\tau_{II}}{2\dot{\varepsilon}_{eff}^{(v)}} \tag{9}$$

In these expressions, τ_{II} is the stress tensor norm defined as the square root of the stress tensor second invariant, R – gas constant, V_a – activation volume and other parameters are material constants.

In the uppermost parts of the lithosphere, temperatures are low, so viscous stresses are extremely high. In this case, maximal stresses are limited by the plastic yield stress, the mechanism simulating brittle faulting. In our model, we employ the Drucker-Prager failure criterion with the non-associative flow rule:

$$f_s = \frac{1}{3} I_1(\sigma)\mu + \tau_{II} - C_h \le 0, \quad g_s = \tau_{II} \tag{10}$$

Here, $I_1(\sigma)$ is the first invariant and τ_{II} is a square root of the second invariant of the stress tensor, g_s – shear plastic flow potential, μ –friction coefficient, and C_h is normalized cohesion.

The angles of friction and cohesion in our model decrease while accumulated plastic strain grows, which is similar to what is assumed in other modeling studies (e.g., Lavier et al., 2000; Huismans and Beaumont, 2002; Babeyko et al., 2002). The functional dependence expressed by the plastic strain softening rule tends to localize strain in the brittle part of the modeled area.

During deformation, the Lagrangian mesh undergoes significant distortion. Since the hybrid Lagrangian-Eulerian computational scheme does not allow considerable grid distortion, we perform the remeshing procedure fairly often. To prevent material properties and stress diffusion during remeshing, we use the Lagrangian markers that track material properties similar to Babeyko et al. (2002) and a full stress tensor like in Sobolev and Babeyko (2005) (see also Babeyko and Sobolev (2005, 2008) for more details). The difference is that here the marker field is three-dimensional. Initially, the markers are uniformly distributed within the modeling area. Between remeshings, we keep the values of the accumulated displacement vector at the grid nodes and use them to calculate new marker coordinates after remeshing.

To decrease the calculation time, we developed a parallel version of the code based on the Message Passing Interface (MPI). We minimize intertask communication traffic using a simplified approach where every processor operates with only one or several

two-dimensional Lagrangian sections. In this case, data transmission between the MPI processes occurs only a few times during the calculation cycle. During data exchanges, every MPI process sends and receives a calculated force contribution, stress and temperature.

2.2 Model setup

We consider a model box of dimensions 100x250x80 km^3, simulating a domain of the continental lithosphere (Fig. 2). The lithosphere consists of a two-layered, 30 km-thick continental crust with a quartz-dominated rheology and an olivine mantle. The corresponding material parameters are listed in Table 1.

In the modeling, we use a tectonic setting similar to the Dead Sea Transform (Garfunkel and Ben-Avraham, 1996), considering the Dead Sea Basin to be a classical pull-apart basin. The model box is subjected to constant left-lateral transform motion at the side boundaries with a velocity of 0.6 cm/yr. To determine an appropriate location and width of a basin in laterally homogeneous media, we introduce two parallel overlapping fault seeds with 12 km spacing (Fig. 2). Seeds are placed in the upper 10 km of the crust and are represented by columns of elements (one-element wide) with initial friction coefficients 2 times smaller than the standard value of 0.5.

The initial temperature distribution is laterally uniform and corresponds to a steady-state continental geotherm with resulting surface heat flow (a model parameter) varying between 40 and 70 mW/m^2.

Because most of the pull-apart sedimentary basins are completely filled with sediments, we assume that all surface depressions deeper than 500 m are filled.

2.3 The plastic softening rule

To help faults localize in the brittle part of the lithosphere, we use frictional plastic strain softening. Assuming that the material softening is not instantaneous, we use a simple approach, where a friction coefficient μ drops proportionally to the accumulated effective plastic strain e^*_{II} similar to Lavier et al. (2000); Huismans and Beaumont (2002) and Babeyko et al.(2002):

$$\mu = k(e^*_{II}) \cdot \mu_0 , \tag{11}$$

$$e^*_{II} = \sqrt{e_{p_{12}}^2 + e_{p_{13}}^2 + e_{p_{23}}^2 - e_{p_{11}}^2 e_{p_{22}}^2 + a^2 e_{p_{33}}^2} . \tag{12}$$

Here, $e_{p_{ij}}$ is the deviatoric part of the plastic strain tensor, parameter ***a*** takes into account the mesh exaggeration along the x_3 axis and compensates for the dependency of the mesh on the measure of strain (typically we take $a = \frac{\Delta x_3}{\Delta x_1}$), and $k(e^*_{II})$ is a piecewise-linear function:

$$k(e^*_{II}) = \begin{cases} 1, & 0 < e^*_{II} < 1 \\ 1 - 0.8 \cdot \dfrac{e^*_{II} - 1}{E_l - 1}, & 1 \le e^*_{II} \le E_l \\ 0.2, & e^*_{II} > E_l \end{cases} , \tag{13}$$

where E_l is a parameter that controls the friction softening rate. We consider a wide range of E_l from E_l =2 (very fast softening) to E_l =12 (slow softening rate).

2.4 Model parameters

Another parameter that we change in our study is the viscosity of the lower crust. Based on laboratory data (Rybacki and Dresen, 2000) that show a relatively strong rheology ("normal" models), we consider another two cases of lower crust viscosity with weaker rheology at the same temperature and stress. In the "weak" and "weakest" models, the parameter B_n in the expression for dislocation creep (eq. 7) is increased by four and eight orders of magnitude, respectively. This leads to a power-law viscosity approximately ten and one hundred times lower at the same strain rate and temperature.

We therefore consider a three-parametric model space, where the initial temperature (initial surface heat flow), lower-crustal viscosity (at the same temperature and stress) and material softening rate vary between models. To reveal the influence of each factor, we divided all numerical experiments into several series. As a reference model, we use a model with an initial surface heat flow of 55 mW/m^2, a "weak" lower crust, and a fast friction softening rate (E_L=2). In every series, we vary only one parameter, all other parameters remaining fixed.

3. Results

Before performing systematic analyses of the various factors that control the structure and evolution of pull-apart basins, we carried out a number of experiments to define

the optimum resolution for our numerical models. Our experiments demonstrated that major features of pull-apart basins, like the basin length, depth of sediments and structure of the underlying lithosphere, are reproduced well even with models with 10 times lower along-strike resolution (see Appendix), which are computationally much less expensive than models with the same resolution in all directions. Therefore, most of the models discussed below are computed assuming 10 times lower resolution along strike than in all other directions.

3.1. Strain rate evolution

The strain rate evolution in our reference model is demonstrated by a series of snapshots in Fig. 3. During the first few million years, the fault seeds grow down and laterally. At the same time, deformation (extension) starts to localize in the region where the faults overlap. At that time, the initial few tens of km-long depression is formed. At this first stage, it is typical to see systems of Riedel shears, and more distributed, rather than strongly localized, deformation patterns. The duration of this first stage depends on the frictional softening rate.

In the case of fast frictional softening, just few million years after strike-slip begins, most of the extension becomes localized between the faults, and an initial depression starts growing parallel to the faults at an almost constant rate. In the case of slow frictional softening (lower section of Fig. 3), the initial stage is strongly prolonged and it may take more than 10 million years before deformation is completely localized in the pull-apart basin.

3.2 Effect of lower crustal viscosity

To illuminate the influence of the lower-crustal viscosity on basin evolution, we created a model series in which we vary only the constant B_n in the dislocation creep expression for the lower crust. We change the pre-multiplier B_n in such a way that the lower crustal viscosity drops by one and two orders of magnitude for the "weak" and "weakest" models, respectively.

Modeling results are similar to our previous ones (Petrunin and Sobolev, 2006). They show that the higher viscosity of the lower crust is, the thicker and deeper the brittle layer and the final sedimentary basin become (Fig. 4). The basin subsidence rate also depends on the viscosity of the lower crust. Models with weaker rheologies show lower subsidence rates. The subsidence rate even becomes negative after 70-90 km of strike-slip displacement for the weakest and weak lower crustal rheologies.

The variation in the lower crustal viscosity is reflected in the shape of the lower-upper crustal boundary (Fig. 5), whereas the change in the shape of the Moho is insignificant. Under a normal lower crustal rheology (Fig. 5a), the sedimentary basin subsides as deep as 22 km. The lower crust is almost completely broken and replaced with upper crustal material, while the Moho boundary has a small depression just beneath the basin. The model with a weak crustal rheology (Fig. 5b) also has a concave flexure at the lower-upper crustal boundary, but the flexure is not as significant. The basin subsidence depth is about 16 km after 100 km of strike-slip displacement and the Moho has a visible uplift of 2-3 km. Unlike the previous two cases, the model with the weakest lower crust (Fig. 5c) is characterized by convex flexure at the lower-upper crustal boundary with an amplitude of about 4 km. The

Moho also has 4-5 km of uplift, but the uplift is broader than in the model with a weak crustal rheology. The sedimentary basin thickness in this model does not exceed 12 km.

3.3 Effect of temperature

In the case of a steady-state initial temperature distribution, the initial surface heat flow directly reflects the thickness of the thermal lithosphere, and as a consequence, the temperature at the Moho and in the lower crust. This series of models includes models with initial surface heat flow varying from 40 to 70 mW/m^2. All other parameters are fixed as in the reference model.

Here we show only three particular cases with initial surface heat flow between 50 and 60 mW/m^2. All models outside this range have similar features as the end-members of the sequence discussed below. As can be seen from Fig. 6, maximal basin subsidence strongly depends on the temperature distribution. Under relatively low initial surface heat flow (50 mW/m^2 and les), the subsidence rate is maximal at the beginning of basin formation and the basin becomes deeper even after 100 km of strike-slip displacement, reaching 20 km depth or more for colder models. The model with relatively high surface heat flow (60 mW/m^2) shows slower basin subsidence and the basin reaches a maximum depth of 12 km at 70 km of strike-slip displacement. Later, the basin depth reduces slightly with time. Models with higher heat flow show a tendency to isostatic compensation, leading to a reduced basin thickness with time.

The lithospheric structure beneath the sedimentary basin changes significantly with temperature (Fig. 7). The main features of the model with low heat flow (50 mW/m^2, Fig. 7a) are very similar to typical features for models with stronger crustal rheology (Fig. 5a). They include intensive basin subsidence (21 km) and considerable lower crustal thinning beneath the basin, expressed by 7 km of subsidence of the lower-upper crustal boundary. Another important feature of the model is a small concave flexure at the Moho. The resulting basin thickness decreases gradually as the initial surface heat flow becomes higher and is equal to 16 and 13 km for models with 55 and 60 mW/m^2, respectively (Figs. 7b, 7c). The lower-upper crustal boundary has only 4 km of subsidence amplitude in the case of moderate heat flow and remains nearly flat for the model with higher surface heat flow. The Moho has a convex flexure that becomes wider and larger in amplitude for higher heat flow.

3.4 Effect of softening rate

Another factor that strongly influences lithospheric rheology is material softening. As is mentioned above (Section 2.3), we use a piecewise-linear softening function parameterized using the softening rate parameter E_l (eq. 11-13). In the model series described above, we used a high softening rate (E_l =2), as in our previous studies (Babeyko et al., 2002; Petrunin and Sobolev, 2006) and similar to the softening rates used in other modeling studies (Lavier et al., 2000; Huismans and Beaumont, 2002), which corresponds to the case when the friction coefficient at the major faults drops to its lowest value (in our case 0.1) in the early stage of basin evolution. However, the rate of strain softening in nature remains uncertain. As a result, we here study the effect of lower softening rates, all other parameters being as in the reference model. In

section 4.4, we will show that the evolution of the Dead Sea Basin is consistent with a relatively low softening rate.

As is shown in Fig. 8, basin evolution is strongly influenced by the softening rate. If the material softening is fast (E_L=2,4, Fig. 8), the pull-apart subsidence rate is high and the basin subsides to16-18 km depth over 80-100 km of strike-slip displacement. In models with a lower softening rate, basin subsidence is lower. Thus, at a moderate softening rate (E_L=8, Fig. 8), it already takes 145 km of displacement along the main faults to reach a maximal basin subsidence of 16 km. Further decreasing the softening rate (E_L=12, Fig. 8) leads to significant changes in the basin evolution. The subsidence rate becomes even lower, and a maximum basin thickness of 12 km is achieved only after 180 km of strike-slip displacement.

The models with fast to moderate softening rates (Fig. 9 a,b,c) have many similarities in lithospheric structure. The thickness of the sedimentary basin ranges from 14 to 16 km, and the Moho uplift is nearly the same and equal to 3-4 km. The concave flexure amplitude at the lower-upper crust boundary degrades as the softening rate decreases. The model with a slow softening rate (Fig. 7d) differs significantly from other models in the series. It is characterized by a shallow sedimentary basin that widens from the bottom to the surface. The resulting basin is only 10 km deep, and it is 2 km wider at the surface than the other basins in the model series. The absence of significant changes at the structural boundaries is also an important distinguishing feature of this model.

3.5 Effect of friction at major faults

In all the above models, friction at major faults bounding the pull-apart basin was assumed to be much lower than friction in the rest of the lithosphere. Here, we explicitly study the effect of the friction at major faults on the evolution of a pull-apart basin of the Dead Sea Basin type.

In all models in this section, there are two overlapping major faults in the central part of the model domain with a prescribed friction coefficient at the faults. As in all other models in this study, the sides of the model domain are subjected to strike-slip displacement with a velocity of 0.6 cm/year. The initial temperature in the models corresponds to initial surface heat flow of 60 mW/m^2, which is probably the highest that can be attributed to the Dead Sea Basin case. Other model parameters are the same as in the reference model.

Fig. 10 shows the distribution of accumulated plastic strain at the surface (left column of figures) and lithospheric structure at strike-perpendicular cross-sections (right column of figures) after 17.5 million years of strike-slip motion, when the total strike-slip displacement approaches 105 km (as in the case of the Dead Sea Basin). If the friction coefficient at the faults is set to 0.3 or 0.4 (compared to 0.5 in the rest of lithosphere), then the faults take up only a small part of the total strike-slip displacement (bottom sections of Fig. 10). As a result, almost no sedimentary basin is formed. The faults take up most of the strike-slip displacement and allow a deep sedimentary basin to form only if the friction at the bounding strike-slip faults is lower than 0.1-0.2 (upper sections of Fig. 10).

The above modeling results demonstrate that a deep pull-apart sedimentary basin can form within relatively cold lithosphere (as in the Dead Sea Basin) only if the friction coefficient at major strike-slip faults is much lower (less than 0.1-0.2) than in the rest of the lithosphere (above 0.5). Otherwise, the strike-slip deformation does not localize at and between the faults but remains distributed within the entire upper crust without forming deep and narrow basins. This result agrees well with the estimation of friction at major faults in lithospheric-scale fault systems like the San Andreas in California (Zoback et al., 1987; Bird and Kong, 1994; Carena, Moder, 2008) and our earlier results for the Dead Sea Transform (Sobolev et al., 2005).

4. Discussion

4.1 The brittle brick stretching (BBS) approach

To summarize all modeling results, let us first consider a major factor that controls the evolution of pull-apart basins, discussed in our previous work (Petrunin and Sobolev, 2006). According to that study, part of the brittle lithosphere, bounded by both transform and transverse faults, accommodates most of the extension within a pull-apart basin. Our current higher-resolution numerical experiments fully confirm that conclusion. Interestingly, the numerical experiments that consider the development of a pull-apart basin in the lithosphere with a complicated visco-elasto-plastic rheology can be described by a simple model that we call Brittle Brick Stretching (BBS). Consider a brick-like brittle domain of the lithosphere bounded by strike-slip faults at its flanks (Fig. 11). Assuming that mechanical decoupling occurs at the sides and lower boundaries of the domain, we set a free-slip boundary condition there. Under

these conditions, the upper free surface subsides as the brittle brick extends. The entire depression is filled with sediments, forming a sedimentary basin. Assume also that the bottom of the brick is fixed. Then, according to mass conservation, the amplitude of the subsidence H_s is proportional to the initial thickness of the brittle layer H_b:

$$H_s = H_b \cdot (1 - L_0/L), \tag{14}$$

where L_0 and L are the initial and current lengths of the layer.

The initial thickness of the brittle layer H_b is controlled by the crustal rheology. Stronger crust has a thicker brittle layer. Thus, according to the BBS approach, the thickness of the sedimentary basin is proportional to the initial thickness of the brittle layer and to the magnitude of strike-slip displacement. This simple relation holds sufficiently well for narrow pull-apart basins within relatively cold lithosphere (see Fig. 5 in Petrunin and Sobolev, 2006). In particular, the BBS model holds if the width of the basin is much smaller than the wavelength of the deformation of the lithosphere related to its flexural rigidity.

The BBS approach can be extended by taking into account the fact that the brittle domain does not have to be continuous with depth. Actually, in our numerical experiments, only end-member models with strongest crust rheology have unified brittle domains reaching 37 km in depth at the initial stages of basin evolution (Table 2). Therefore, we define H_b in eq. 14 as the sum of the thicknesses of all brittle domains within the lithosphere, similar to the approach by Burov and Diament (1995). With this assumption, there is generally good agreement between the basin subsidence depth observed in the numerical experiments and that estimated with the BBS

approach for models with fast softening rates, relatively low initial surface heat flow, and normal or moderately weak rheology of the lower crust (Figs. 4-8, Table 2). However, the BBS approach does not work when the surface heat flow is high (i.e. temperature of the uppermost mantle lithosphere is high) or/and lower crustal rheology is very weak (see numbers in italics in Table 2). For example, in the case of weakest rheology of the lower crust and a relatively low heat flow of 50 mW/m^2, the mantle lithosphere has an 8 km brittle layer, but this layer does not significantly influence basin subsidence because there is efficient decoupling between the crust and mantle due to very low lower crustal viscosity. In this case, the BBS approach holds again, if only the brittle layer in the upper crust (but not in the mantle) is considered. Basin thickness estimated from the BBS approach under that assumption is given in brackets in Table 2.

4.2 End-member scenarios for basin evolution

A simple BBS model obviously does not take into account several important factors. First, it ignores isostatic compensation of the basin, although a thick layer of relatively low density sediments has significant negative buoyancy. Second, the BBS model assumes that the entire deformation is localized between the faults, which may not be the case if faults are not very weak. In a way, the BBS model is one end-member case valid if (i) lithospheric rigidity is high enough to prevent significant isostatic compensation of the narrow basin, and (ii) faults bordering the basin are weak enough to prevent "leaking" of the deformation out of the basin. Assuming that the mantle lithosphere viscosity is high enough to prevent significant Moho uplift, we

can propose a number of end-member scenarios for basin evolution, the BBS model being one of them.

Let us consider a case (Fig. 12) in which the lower boundary of the brittle layer is located within the lower crust and the viscosity of the ductile crust is high. In this case, viscous forces are high and they prevail over negative loading of the sedimentary basin. This means that the bottom of the brittle brick remains fixed for a long time and BBS approach relation (14) is applicable. In this case, subsidence of the lower-upper crustal boundary ΔH_{lc} is expressed by the following relation:

$$\Delta H_{lc} = (H_b - H_{uc}) \cdot (1 - L_0 / L), \tag{15}$$

where H_{uc} is the initial upper crustal thickness, which can be defined as the thickness of the upper crust outside the basin.

Another end-member case assumes complete isostatic compensation of the basin, which holds if the lithospheric rigidity cannot sustain the large negative load implied by the basin. In this case, the brittle brick will go up, as shown in Fig. 13, according to Airy isostasy; the thickness of the sediments will be:

$$H_{sed} = H_{uc} \cdot (1 - L_0 / L) \cdot (\rho_l - \rho_u) / (\rho_l - \rho_s), \tag{16}$$

where ρ_u, ρ_l and ρ_s are upper and lower crust and sedimentary densities. It is interesting that in this case the basin thickness does not depend on the initial brittle layer

thickness since the brittle part of the lower crust has no density contrast with the ductile part. The lower-upper crustal boundary rise in this case will be:

$$\Delta H_{lc} = H_{uc} \cdot (1 - L_0/L) \cdot (\rho_u - \rho_s)/(\rho_l - \rho_s)\,. \qquad (17)$$

For narrow (10-15 km wide) basins like the Dead Sea Basin, this scenario is valid only for models with very weak crustal rheologies.

Actually, the real case is a combination of the two end-members described above (Fig. 15). For strike-slip displacement of about 100 km or less achieved in less than 20 million years, the narrow (12 km wide) pull-apart basin subsides in a mode very close to that described by the BBS model if the initial surface heat flow is less than 70 mW/m^2 and strain softening at the faults is rapid. However, if strike-slip occurs for a longer time, or the lithospheric temperature (surface heat flow) is much higher, then viscous flow in the lower crust tends to push up the light brittle block containing sedimentary basin, restoring the isostatic equilibrium.

In the special case of a very cold lithosphere (Figs. 5a, 7a), the brittle layer may become thicker than the crust (Fig. 14). Assuming that the mantle lithosphere below the brittle-ductile transition is strong enough to keep the lower boundary of the brittle layer stable for a long time, we can use expression (14) to estimate the displacement of the Moho (ΔH_M):

$$\Delta H_M = (H_b - H_{lc} - H_{uc}) \cdot (1 - L_0/L)\,. \qquad (18)$$

As the Moho in this case is located within the brittle brick, it will subside during deepening of the pull-apart sedimentary basin, contrary to what happens in the case of a basin formed by rifting. Thus, for the models presented in Figs. 5a and 7a, the BBS model predicts about 4 km of Moho subsidence, which is reasonably close to the numerical results.

Another special case is if the lithosphere is extremely weak and only the upper part of the upper crust is brittle while the underlying ductile upper crust has very low viscosity. In this case, the bottom of the deforming brittle brick will rise and the thickness of the sedimentary basin will be much smaller than predicted by BBS model. Note that if mantle viscosity is low enough, the Moho will tend to uplift in this case.

In the previous discussion, we considered only the case of a high softening rate in which the friction coefficient minimum was achieved at relatively small strain. This means that faults bordering the basin became frictionally weak in the beginning of basin growth and since that time all the deformation was localized within the basin. In the case of a slow softening rate, the faults remain rather strong for a long time, which leads to “leaking” of the deformation out of the basin. Therefore, elongation of the basin appears to be smaller than strike-slip displacement. As long as the basin subsidence due to brittle brick stretching depends on elongation, and the degree of viscous compensation depends on time, other conditions being equal, isostatic compensation plays a more significant role in the slow softening rate models, with more isostatic compensation and a shallower basin in Fig. 9cd than Fig. 9ab (see also Fig. 8).

4.3 Models consistent with the Dead Sea basin

Using the simple models described above, it is possible to make predictions concerning the internal structure and rheology of a pull-apart basin based on geological and geophysical data. For instance, the distribution of seismicity under the Dead Sea Basin (DSB) has a clear maximum at a depth around 18 km according to the relocated event data by Shamir (2006), which is slightly less than previous estimates (22 km) by Aldersons et al. (2003). Maximum energy release in the regions of high strain rate occurs at the bottom of the brittle layer, where the stress is maximal. The thickness of the brittle layer of about 18-22 km according to the BBS model corresponds to the maximum thickness of the Cenozoic sedimentary layer of 12-14 km. This value is slightly above the observed thickness (10 km) of the Dead Sea Basin along the DESIRE line crossing the basin at the point of the largest Bouguer gravity anomaly. This probably indicates that either some minor isostatic compensation of the basin occurred, or the frictional softening rate was rather slow, or both.

Geological data shows that the present subsidence rate is high (0.8–0.9 mm/yr) within the bounds of the DSB (Kaufmann et al., 1992; Marco et al., 1994; Abu-Jaber et al., 1997). This constraint allows us to reject models with low or negative subsidence rates, i.e. models with fast softening rates and weakest rheologies. Geophysical observations also suggest no significant flexure at the upper-lower crustal boundary and at the Moho boundary beneath the DSB (Mechie et al., 2005; ten Brink et al.,

2006). Only models with a slow softening rate meet this condition (see Fig. 9d) if the initial surface heat flow is less than 60 mW/m^2, as in the case of the DSB (Ben-Avraham et al., 1978; Eckstein and Simmons, 1979). We therefore conclude that the best fitting models for the DSB are those with a relatively slow softening rate and weak to normal lower crustal rheology.

Finally, we use our modeling results to estimate a possible friction coefficient at major faults bounding the DSB. According to our models presented in section 3.5 (see also Fig. 10), the friction coefficient at major faults of the DSB must be rather low (lower than 0.1-0.2) in order to allow the formation of a deep, long and narrow sedimentary basin within relatively cold lithosphere. We note that in the models of section 3.5 we considered lithosphere with initial heat flow of 60 mW/m2, which is likely the highest that can be expected for the DSB. If in fact the lithosphere there is colder (Ben-Avraham et al., 1978; Eckstein and Simmons, 1979), the friction at the major faults must be even lower than 0.1 to enable formation of the DSB.

5. Concluding remarks

We have created a series of thermomechanical models of a pull-apart basin growing at a stepping of a transform fault due to progressive strike-slip motion. All models incorporate a non-linear temperature- and stress dependent visco-elasto-plastic rheology with parameters consistent with laboratory measurements.

We consider a three-parametric model space, where the initial temperature (initial surface heat flow), lower-crustal viscosity (at the same temperature and stress) and material softening rate vary between models.

The modeling shows that basin subsidence results from the competition of extension of the brittle part of the lithosphere, which leads to subsidence, and of compensational flow of the deeper ductile part of the lithosphere, which pushes the extended brittle block upwards. The result of this competition, i.e. the subsidence rate, and crustal structure are controlled by (i) the thickness of the brittle layer and basin width, (ii) the magnitude of strike-slip displacement, (iii) the rate of frictional softening of the crust and (iv) the viscosity of the ductile part of the lithosphere. The thickness of the brittle layer and the viscosity of the underlying ductile part of the lithosphere in turn depend on temperature, composition and material softening.

The results of most of our numerical experiments can be described by a simple analytical model that we call the brittle brick stretching (BBS) approach. According to this model, basin subsidence is driven by uniform fault-parallel stretching of the brittle part of the lithosphere bordered by the overlapping segments of the transform fault (brittle brick) with a fixed lower bottom. According to the BBS approach, the thickness of the sedimentary basin is proportional to the initial thickness of the brittle layer and the magnitude of strike-slip displacement. We demonstrate that the BBS model gives an upper-limit estimate of the thickness of the sedimentary basin, which is closely approached if the lithosphere is relatively cold (initial surface heat flow less than 70 mW/m^2), the basin develops over less than 20 million years and the friction

softening rate is high (i.e. basin-bordering faults become weak in the beginning of basin formation).

We also demonstrate that the structure and evolution of the Dead Sea Basin, located at a left stepping of the Dead Sea Transform in the Middle East, is consistent with BBS-type deformation with only a minor contribution of compensational flow in the ductile part of the lithosphere.

Finally, we show that the formation of a narrow and deep pull-apart basin in relatively cold lithosphere like the Dead Sea Basin requires very low friction at major faults (lower than 0.1-0.2). If this condition is not satisfied, strike-slip deformation does not localize at and between the overlapping faults, and a deep basin does not form.

Acknowledgments

AP was funded by the Deutsche Forschungsgemeinschaft in the framework of the DESIRE Project. We appreciate useful discussions with the members of the DESIRE team and constructive comments of the PEPI editors and anonymous referees.

References

Abu-Jaber, N.S., Al-Bataina, B.A. and Jawad Ali, A., 1997, Radiochemistry of sediments from the southern Dead Sea, Jordan. Env. Geol., 32:281-284.

Aldersons, F., Ben-Avraham, Z., Hofstetter, A., Kissling, E., and Al-Yazjeen, T., 2003, Lowercrustal strength under the Dead Sea basin derived from local

earthquake data and rheological modelling: Earth and Planetary Science Letters, v. 214, p. 129–142, doi: 10.1016/S0012-821X(03)00381-9.

Atmaoui, N., Kukowski, N., Stöckhert, B. and König, D., 2006, Initiation and development of pull-apart basins with Riedel shear mechanism: Insight from scaled clay experiments. - International Journal of Earth Sciences 95: 225-238.

Aydin, A.A., and Nur A., 1985, The types and roles of stepovers in strike-slip tectonics, *in* K.T. Biddle and N. Christie-Blick, eds., Strike-slip deformation, basin formation, and sedimentation: SEPM Special Publication 37, p. 35-45.

Babeyko, A.Y., Sobolev,S.V., Trumbull,R.B., Oncken,O., and Lavier,L., 2002, Numerical models of crustal scale convection and partial melting beneath the Altiplano-Puna plateau, Earth and Planetary Science Letters,199,3-4,373-388.

Babeyko, A.Y., and Sobolev, S. V. ,2005, Quantifying different modes of the late Cenozoic shortening in the central Andes, Geology, 33, 8, 621-624.

Babeyko, A.Y., and Sobolev S.V., 2008, High-resolution numerical modeling of stress distribution in visco-elasto-plastic subducting slabs, Lithos, 103, 1-2., doi:10.1016/j.lithos.2007.09.015

Ben-Avraham, Z. and M.D. Zoback, 1992. Transform-normal extension and asymmetric basins: An alternative to pull-apart models, Geology, 20, 423-426.

Ben-Avraham, Z., Haenel, R., and Villinger, H., 1978, Heat flow through the Dead Sea rift: Marine Geology, v. 28, p. 253–269, doi: 10.1016/0025-3227(78)90021-X.

Burchfiel, B. C., and J. H. Stewart, 1966, "Pull-apart" origin of the central segment of Death Valley, California: GSA Bull., v. 77, pages 439-442.

Burov E and Diament M , 1995, The effective elastic thickness of continental lithosphere: What does it really mean? J. Geophys. Res.,100, 3905-3927

Christie-Blick, N., and K.T. Biddle, 1985, Deformation and basin formation along strike-slip faults, *in* K.T. Biddle and N. Christie-Blick, eds., Strike-slip deformation, basin formation, and sedimentation: SEPM Special Publication 37, p. 1-35.

Crowell, J.C., 1974, Origin of late Cenozoic basins in southern California, *in* R.H. Dott and R. H. Shaver, eds., Modern and ancient geosynclinal sedimentation: SEPM Special Publication 19, p. 292-303.

Eckstein, Y., and Simmons, G., 1979, Review of heat flow data from the eastern Mediterranean region: Pure and Applied Geophysics, v. 117, p. 150–159.

Garfunkel, Z. 1981. Internal structure of the Dead Sea leaky transform (rift) in relation to plate kinematics. Tectonophysics, 80, 81–108.

Garfunkel, Z. and Z. Ben-Avraham, 1996, The structure of the Dead Sea basin, Tectonophys., 266, 155-176.

Gleason, G.C., and Tullis, J., 1995, A flow law for dislocation creep of quartz aggregates determined with the molten salt cell: Tectonophysics, v. 247, p. 1–23, doi: 10.1016/0040-1951(95)00011-B.

Hirth, G. & Kohlstedt, D. L. 1996. Water in the oceanic upper mantle: implications for rheology, melt extraction and the evolution of the lithosphere. Earth and Planetary Science Letters, 144, 93–108.

Huismans, R.S., and Beaumont, C, 2002, Asymmetric lithospheric extension: the role of frictional plastic strain softening inferred from numerical experiments,

Geology, 30, 3, 211-214.

Kameyama, M., D. A.Yuen, and S.-I. Karato. 1999, Thermal-mechanical effects of low-temperature plasticity (the Peierls mechanism) on the deformation of a viscoelastic shear zone: Earth and Planetary Science Letters. 168,159-172.

Katzman, R., U. ten Brink, and J. Lin. 1995, Three-dimensional modeling of pull-apart basins; implications for the tectonics of the Dead Sea basin: Journal of Geophysical Research. 100,6295-6312.

Kaufman, A., Yechieli, Y., and Gardosh, M., 1992. Reevaluation of the lake-sediment chronology in the Dead Sea basin, Israel, based on new 230Th/U dates. Quat. Res. 38, 292-304

Lavier, L., W., Buck, and A. Poliakov (2000), Factors controlling normal fault offset in an ideal brittle layer, J. Geophys. Res., 105(B10), 23431-23442.

Le Calvez, J. H. and Vendeville, B. C. 2002. Experimental designs to model along-strike fault interaction. In: Schellart, W. P. and Passchier, C. 2002. Analogue modelling of large-scale tectonic processes. Journal of the Virtual Explorer, 7, 7-23.

Marco, S., Agnon, A., Stein, M., Ron, H., 1994. A 50,000 years continuous record of earthquakes and surface ruptures in the Lisan Formation, the Dead Sea Graben. United States Geological Survey Open-File Report 94-568, pp. 112–114.

McClay, K., and T. Dooley, 1995, Analog models of pull-aparts: Geology, v. 23, p. 711-714.

McClay, K. and M. Bonora, 2001, Analogue models of restraining stepovers in strike-slip fault systems. Bulletin of the American Association of Petroleum Geologists. V.85, No. 2, 233 - 260.

Mechie, J.; Abu-Ayyash, K.; Ben-Avraham, Z.; El-Kelani, R.; Mohsen, A.; Rümpker, G.; Saul, J.; Weber, M. ,2005, Crustal shear velocity structure across the Dead Sea Transform from two-dimensional modelling of DESERT project explosion seismic data, Geophysical Journal International, 160, 3, 910-924.

Petrunin, A.; Sobolev, S. V.,2006, What controls thickness of sediments and lithospheric deformation at a pull-apart basin?, Geology, 34, 5, 389-392.

Rahe, B., D. A. Ferrill, and A. P. Morris,1998, Physical analog modeling of pull-apart basin evolution, Tectonophysics, *285*, 21–40

Richard, P. D., Naylor, M. A., and Koopman, A, 1995, Experimental models of strike slip tectonics, Petroleum Geoscience, 1, 71–80.

Rodgers, D.A., 1980, Analysis of pull-apart basin development produced by en echelon strike-slip faults: Spec. Pub. Internat. Assoc. Sedimentologists, n. 4, p. 27-4

Rybacki, E., Dresen, G., 2000, Dislocation and diffusion creep of synthetic anorthite aggregates: Journal of Geophysical Research, 105, p. 26017–26036, doi: 10.1029/2000JB900223.

Segall, P., and D. D. Pollard (1980), Mechanics of discontinuous faults, J. Geophys. Res., 85, 4337– 4350.

Shamir G, 2006, The active structure of the Dead Sea Depression. Special Paper 401: New Frontiers in Dead Sea Paleoenvironmental Research: Vol. 401, No. 0 pp. 15–32

Smit, J., 2005, Brittle-ductile coupling in thrust wedges and continental transforms, [Ph.D. thesis]: Free University, Amsterdam.

Sobolev, S. V., and A.Y. Babeyko, 2005, What drives orogeny in the Andes?, Geology, 33, 8, 617-620.

Sobolev, S.V., Petrunin, A., Garfunkel, Z., Babeyko, A. Yu., and DESERT Group, 2005, Thermomechanical model of the Dead Sea transform: Earth and Planetary Science Letters, v. 238, p. 78–95.

Sylvester, A.G., 1988, Strike-slip faults: Geological Society of America Bulletin, v. 100, p. 1666-1703.

ten Brink, U.S., Al-Zoubi, A.S., Flores, C.H., Rotstein, Y., Qabbani, I., Harder, S.H., and Keller, G.R., 2006, Seismic imaging of deep low-velocity zone beneath the Dead Sea basin and transform fault; Implications for strain localization and crustal rigidity: Geophysical Research Letters, v. 33, no. 24, p. L24314.

ten Brink, U.S., Katzman, R., and Lin, J., 1996, Three-dimensional models of deformation near strike-slip faults: Journal of Geophysical Research, v. 101, p. 16,205–16,220, doi: 10.1029/96JB00877.

Twiss, R.J., and E.M. Moores. 1992. Structural Geology. New York: W.H. Freeman and Company.

Figure captions

Fig. 1. Schematic representation of the coupled FE-FD spatial discretization.

Fig. 2 Model setup.

Fig. 3. Time snapshots of the strain rate distribution of the evolution of the pull-apart basin.

Fig. 4. Maximum thickness of sediments versus strike-slip displacement along major faults for models with different lower crustal viscosities, the same initial surface heat flow of 55 mW/m^2 and the same fast friction softening rate (E_L=2).

Fig. 5. Lithospheric structure for models with different lower crustal viscosities, the same initial surface heat flow of 55 mW/m^2 and the same fast friction softening rate (E_L=2) after 100 km of strike-slip displacement.

Fig. 6. Maximum thickness of sediments versus strike-slip displacement along the main faults for models with different surface heat flows, the same "weak" lower crustal rheology and the same fast friction softening rate (E_L=2).

Fig. 7. Lithospheric structure for models with different surface heat flows, the same "weak" lower crustal rheology and the same fast friction softening rate (E_L=2) after 100 km of strike-slip displacement.

Fig. 8. Maximum thickness of sediments versus strike-slip displacement along the main faults for models with different softening rates and the same “weak” lower crustal rheology.

Fig. 9. Lithospheric structure for models with different softening rates and the same “weak” lower crustal rheology after 100 km of strike-slip displacement.

Fig. 10. Influence of friction at major faults on the structure of a pull-apart basin. Left column shows the distribution of accumulated plastic strain at the surface and right column shows crustal structures for the models with different friction at major faults after 105 km of strike-slip displacement at the side boundaries.

Fig. 11. Brittle brick stretching (BBS) model.

Fig. 12. Evolution of the structure of the crust subjected to stretching for the case when the lower boundary of the brittle layer is located within the lower crust and is fixed because of the high viscosity of the lower crust (BBS model).

Fig. 13. Evolution of the structure of the crust subjected to stretching for the case when the lower boundary of the brittle layer is located within the lower crust and complete isostatic compensation is achieved.

Fig. 14. Evolution of the structure of the lithosphere subjected to stretching in the case when the Moho is located within the brittle layer.

Fig. 15. Characteristic depth of the basin versus accumulated strike-slip displacement. The actual depth of the basin (thick dashed curve) plots below the BBS approximation (upper curve) and above the full isostatic compensation approximation (lower curve). Thin dashed lines mark asymptotic solutions for the end-member cases (eqs. 14, 16) at infinite elongation of the pull-apart basin.

Fig. A1. Distribution of the second invariant of strain rate and resulting crustal structure after 100 km of strike-slip in models computed with different resolutions in the direction of strike-slip motion. The left column shows a plain view and the middle and right columns show the middle cross-sections perpendicular to the strike-slip direction. The resolution increases twice for every row from 10 to 2.5 km mesh step in the slip direction.

Appendix. Effect of numerical resolution on modeling results.

Fig. A1 demonstrates the modeling results for different resolutions parallel to the strike. While the fine structure of the deformation field significantly depends on the numerical resolution, the major features of the models, like depth and length of the basin and structure of the lithosphere below the basin, are basically the same in the models with different resolutions parallel to the strike direction. This justifies our use of models with lower resolutions for our analyses.

Table 1
Material parameters

Parameter	Sediments	Upper crust	Lower crust	Mantle
Density, ρ, (kg/m^3)	2200	2750	2950	3280
Thermal expansion, $\alpha \times 10^5$, (K^{-1})	3.7	3.7	2.7	3.0
Elastic moduli, K; G, (GPa)	55; 36	55; 36	63; 40	122; 74
Heat capacity, C_p, (J/kg/K)	1200	1200	1200	1200
Heat conductivity, λ, (W/K/m)	2.0	2.5	2.5	3.3
Heat productivity, A, (μW/m^3)	1.3	1.3	0.2	0
Initial cohesion, C_h, (MPa)	20	20	20	40
Strain softening: cohesion	70% at 0 to 10% strain	70% at 0 to 10% strain	70% at 0 to 10% strain	90% at 0 to 10% strain
Initial friction coefficient, μ	0.5	0.5	0.5	0.5
Strain softening: friction	See 2.3, eq. 11-13			-
Pre-exponential constant for dislocation creep, log(B_n), (Pa^{-n}s^{-1})	-28.0[(1)]	-28.0[(1)]	"normal" -15.4[(2)] "weak" -12.4 "weaker" -9.4	-16.3[(3)]
Power law exponent, n	4.0[(1)]	4.0[(1)]	3.0[(2)]	3.5[(3)]
Activation energy for dislocation creep, E_n,(kJ/mol)	223[(1)]	223[(1)]	356[(2)]	535[(3)]
Activation volume, (cm^3)	15	15	15[(2)]	15[(3)]

Dislocation creep law parameters:
[(1)] Gleason and Tullis (1995)
[(2)] Rybacki and Dresen (2000)
[(3)] Hirth and Kohlstedt (1996)
Source for diffusion and Peierls' creep laws in mantle: Kameyama et al. (1999).

Table 2
Modeling results versus BBS estimations

Lower crust	Surface heat flow, mW/m^2	Thickness of the brittle layer, km			Basin subsidence, km (after 100km of strike-slip)	
		crust		upper mantle	according to "BBS" approximation	computed
		upper	lower			
normal	50	39			22.9	21.5
	55	37			23.5	24
	60	15	7	1-2	16.8	16.2
	70	*12*	*1*	-	*9.8*	*5.9*
weak	50	25		8	22.6	20
	55	22		3	17.4	16
	60	16	1-2	<1	12.7	13
	70	*11.3*	*<1*	-	*8.2*	*5.6*
weakest	50	20.5		8	17.1(12.3)	12
	55	19		<1	13	13
	60	*16*		-	*11.2*	*9*

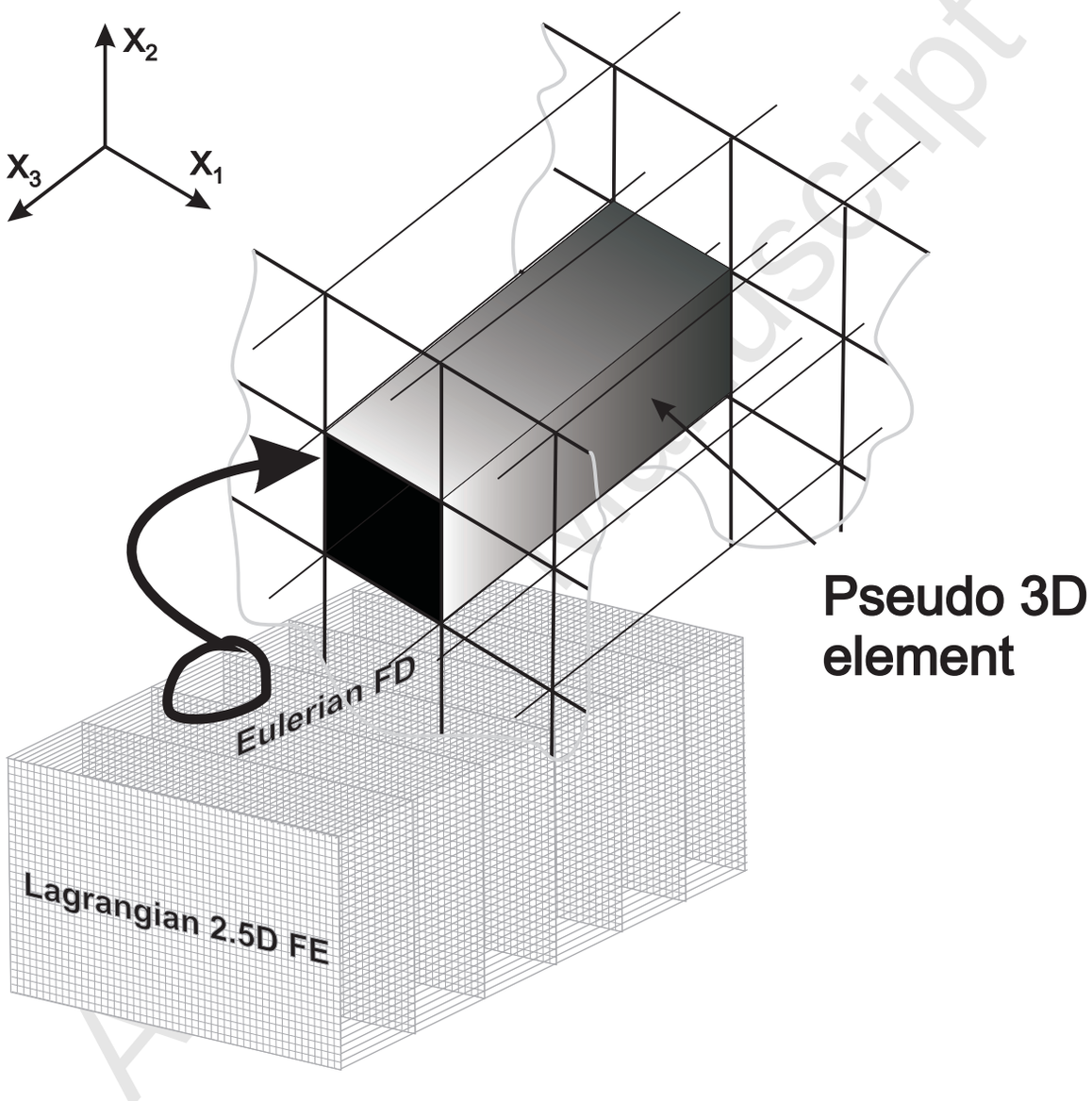

Fig.1

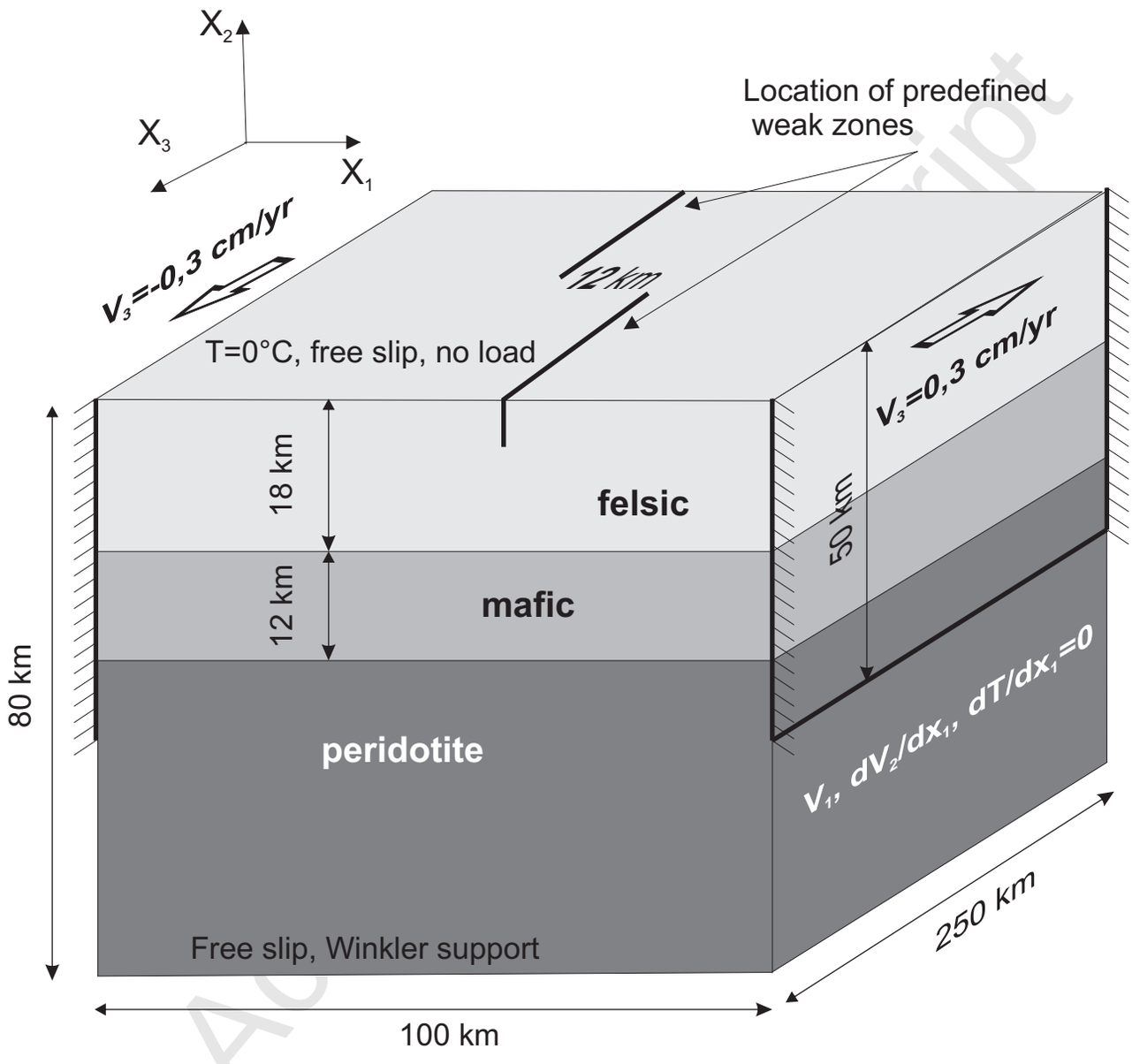

Fig.2

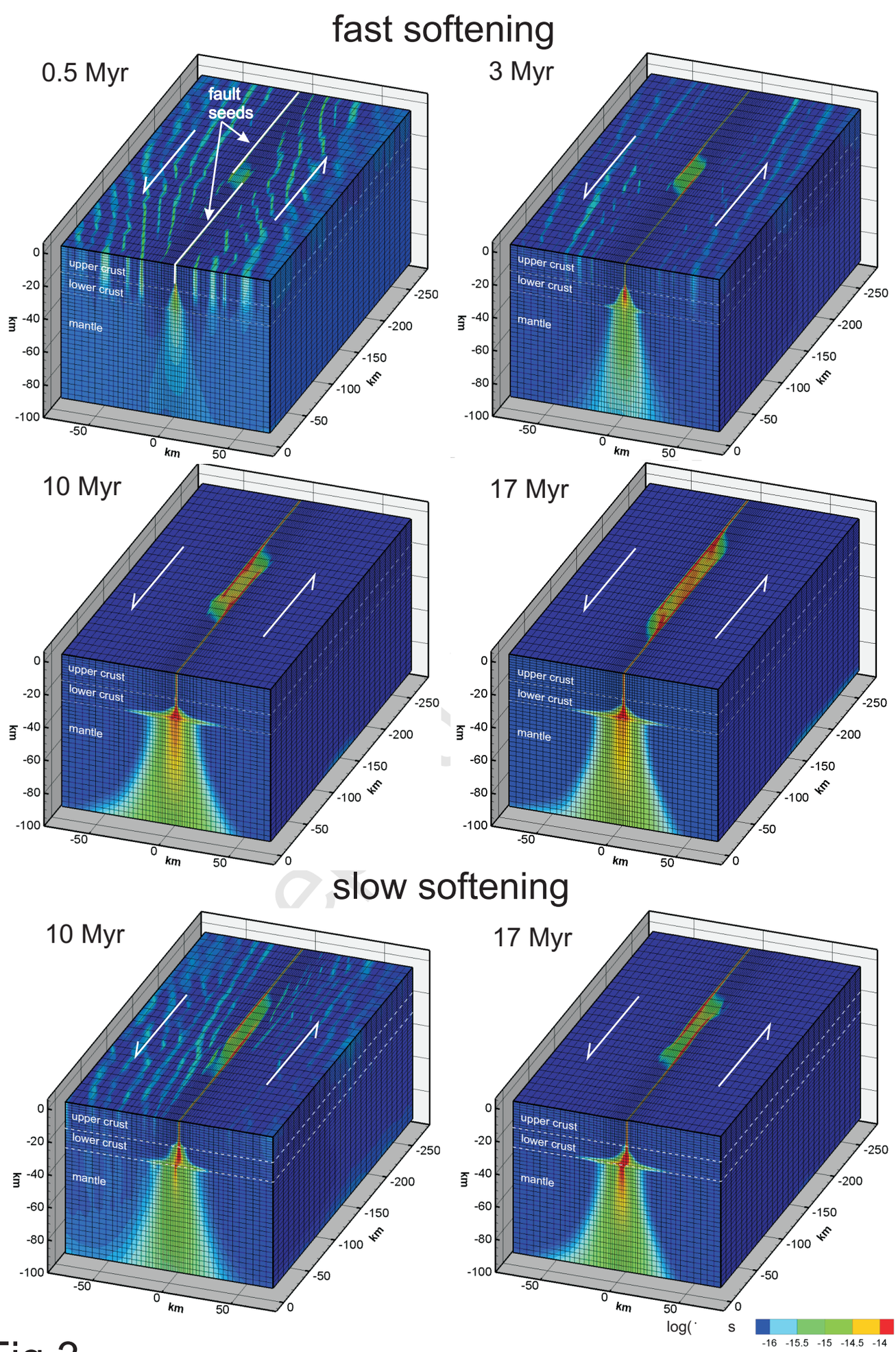

Fig.3

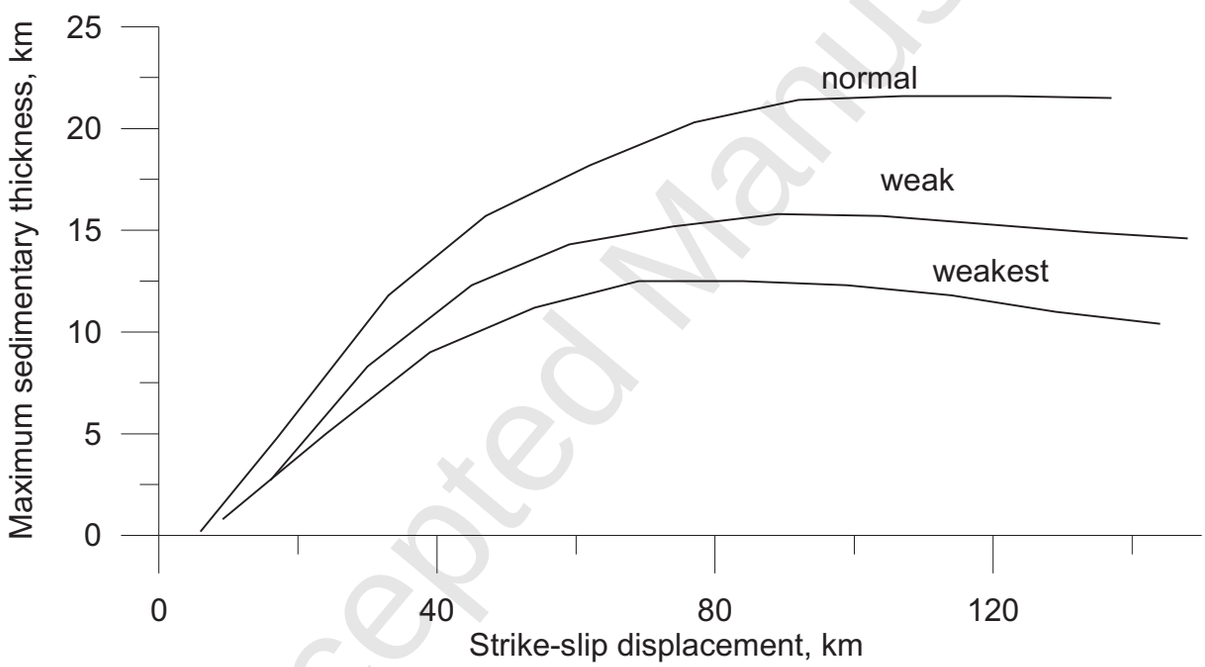

Fig.4

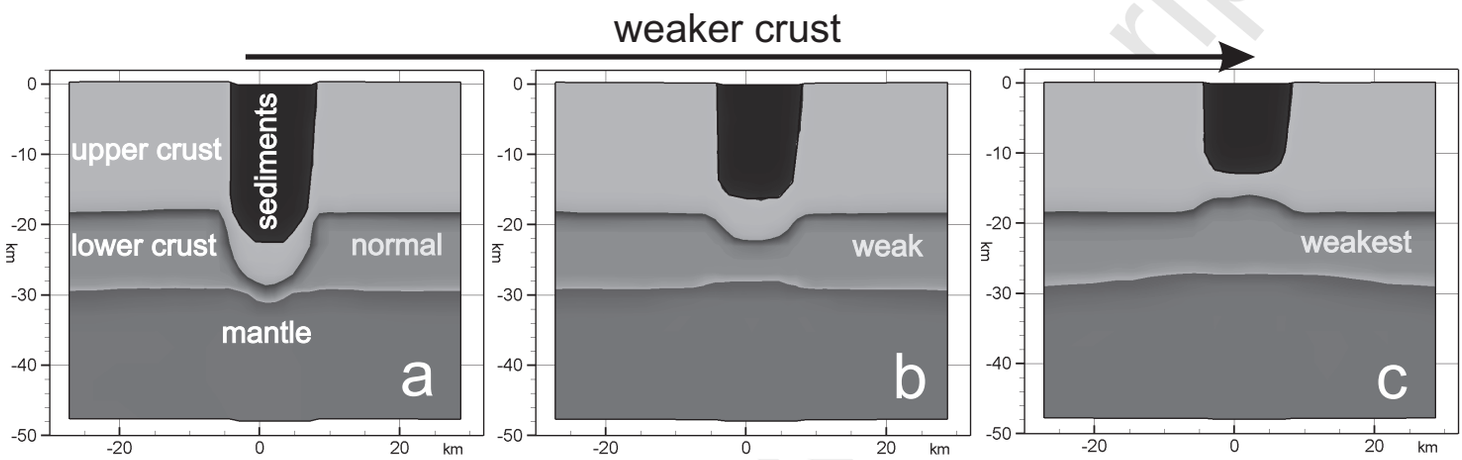

Fig.5

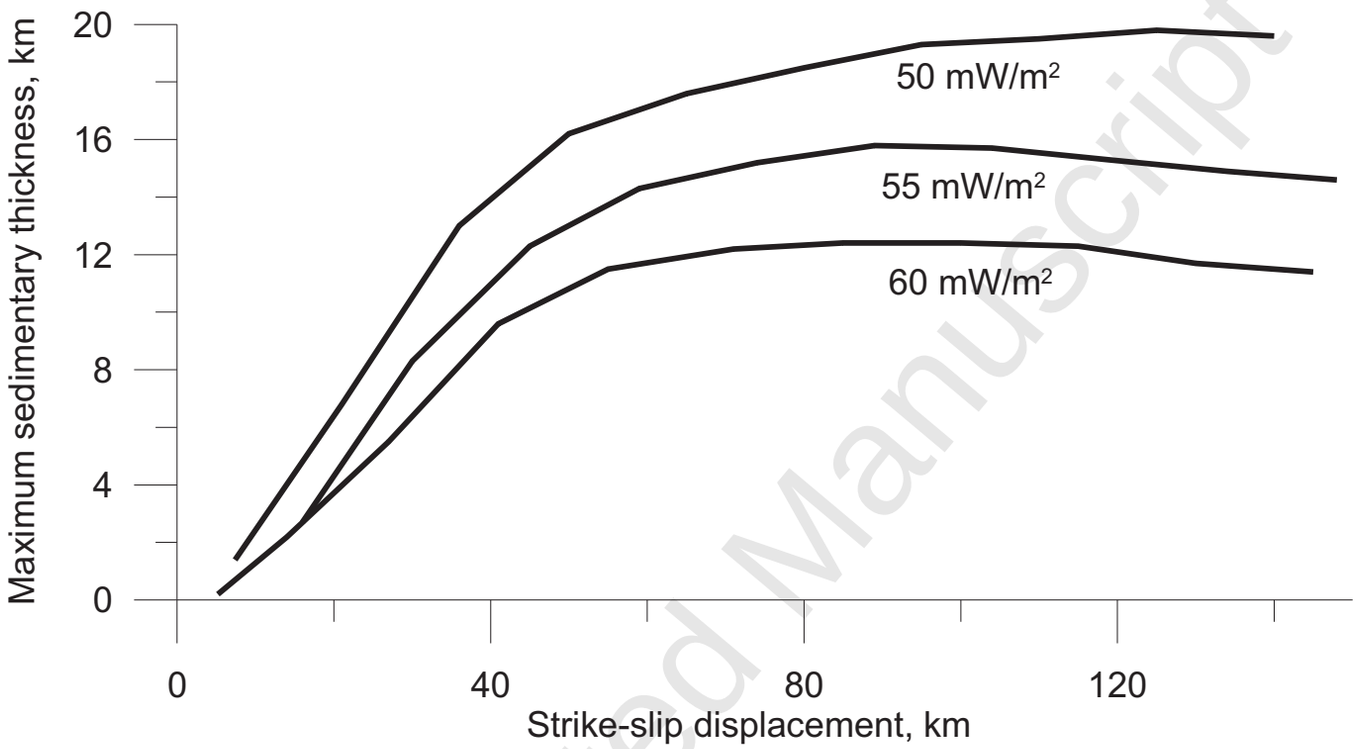

Fig.6

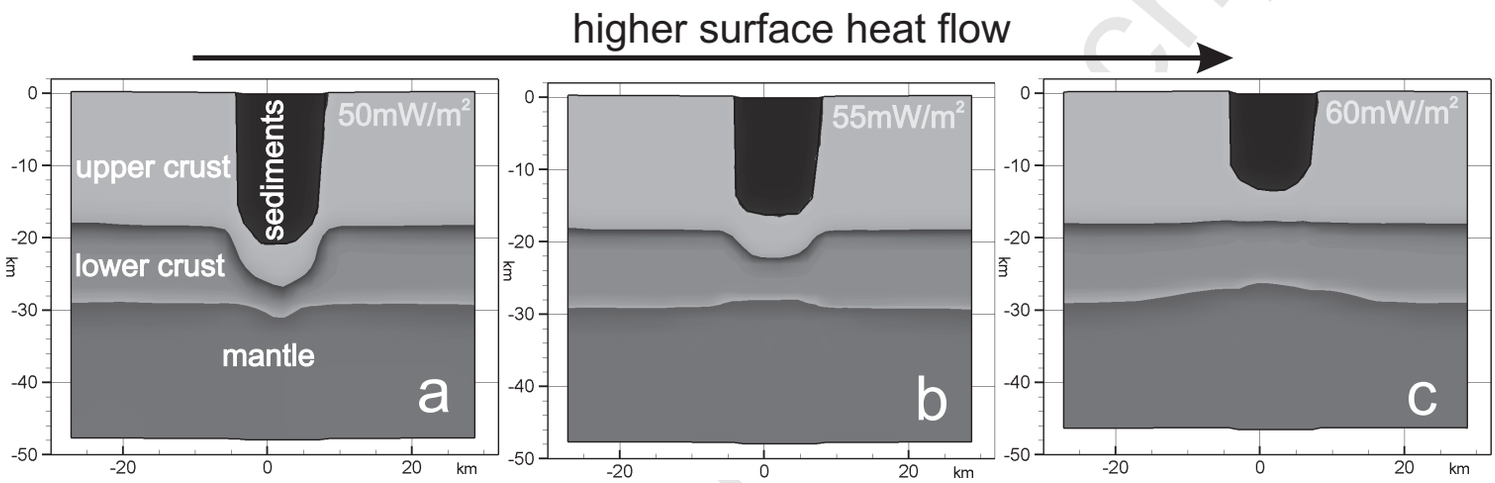

Fig.7

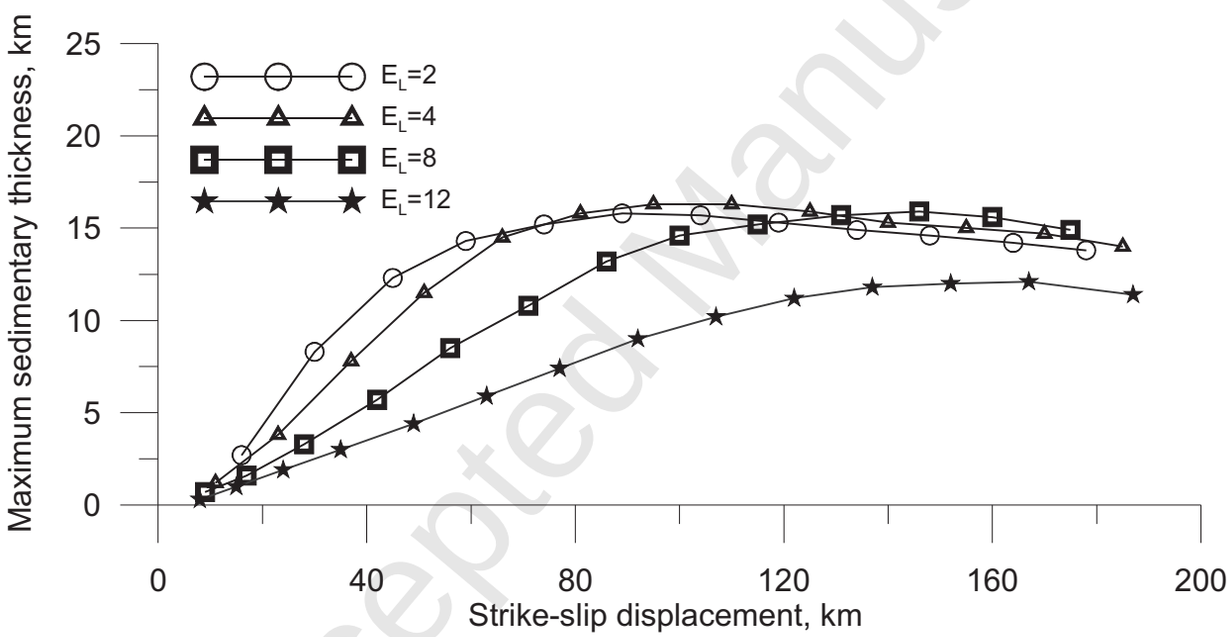

Fig.8

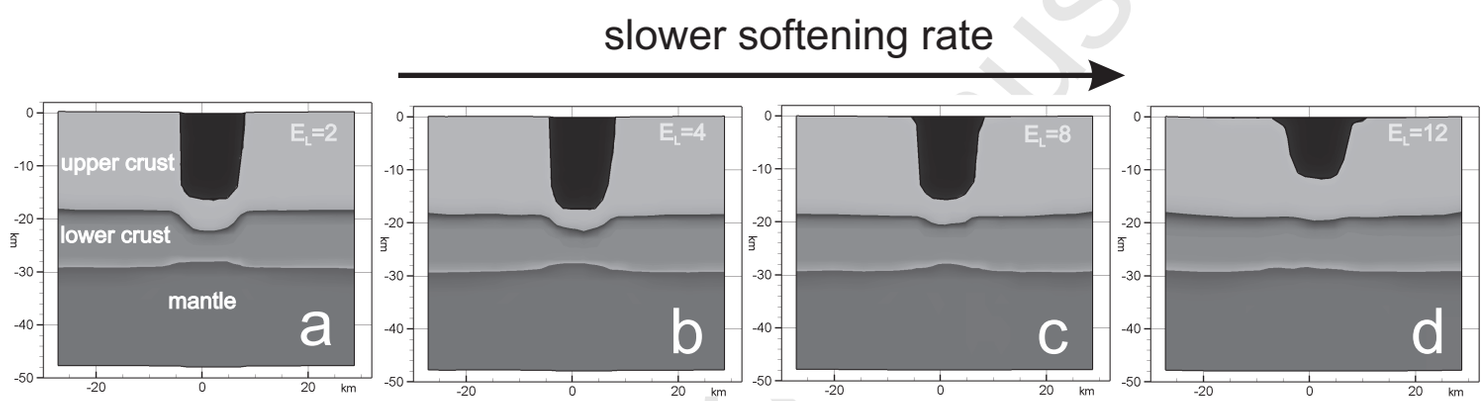

Fig.9

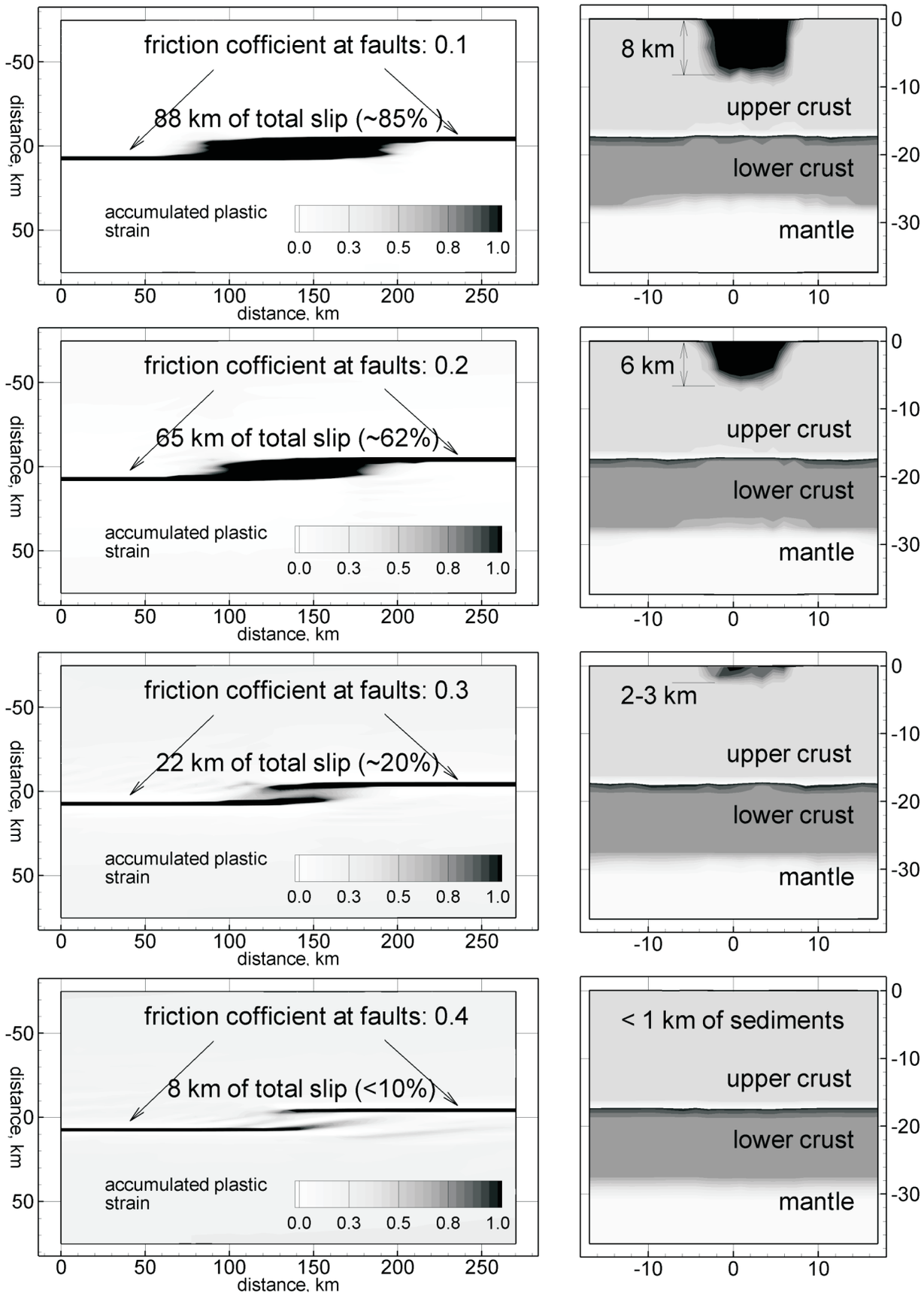

Fig.10

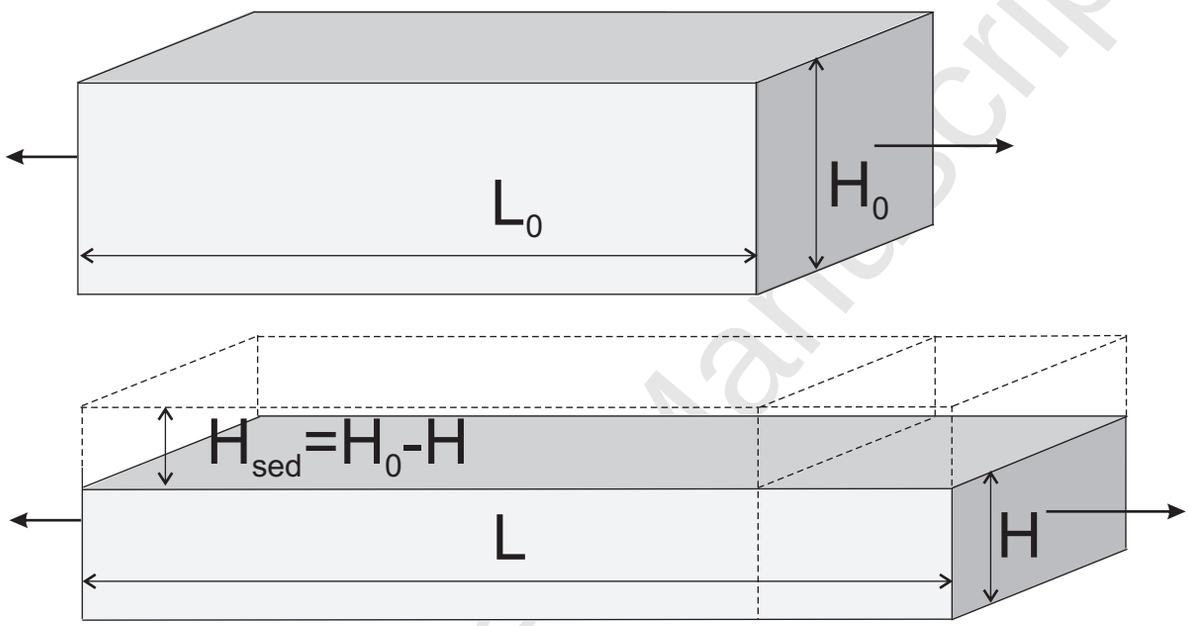

Fig.11

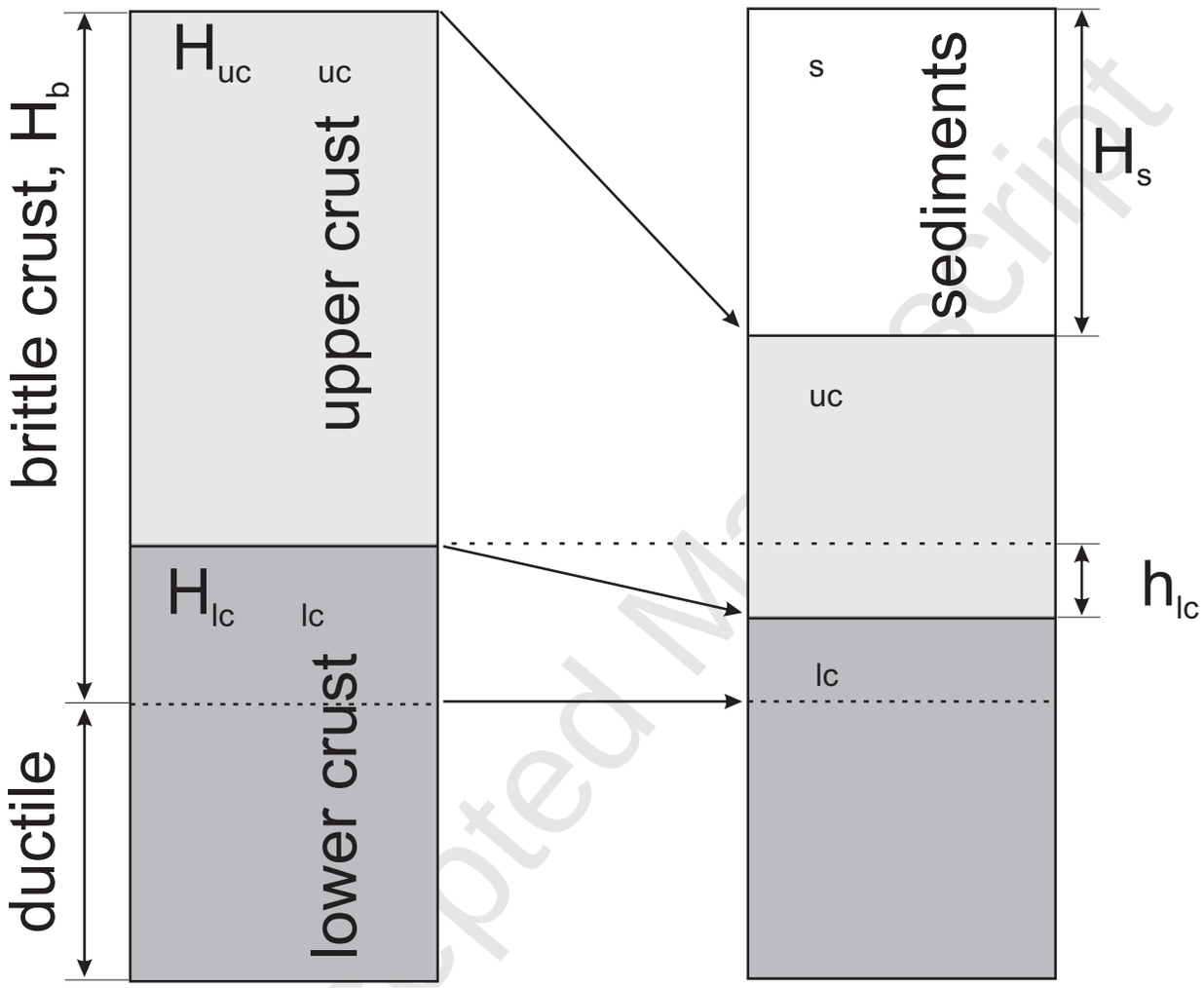

Fig.12

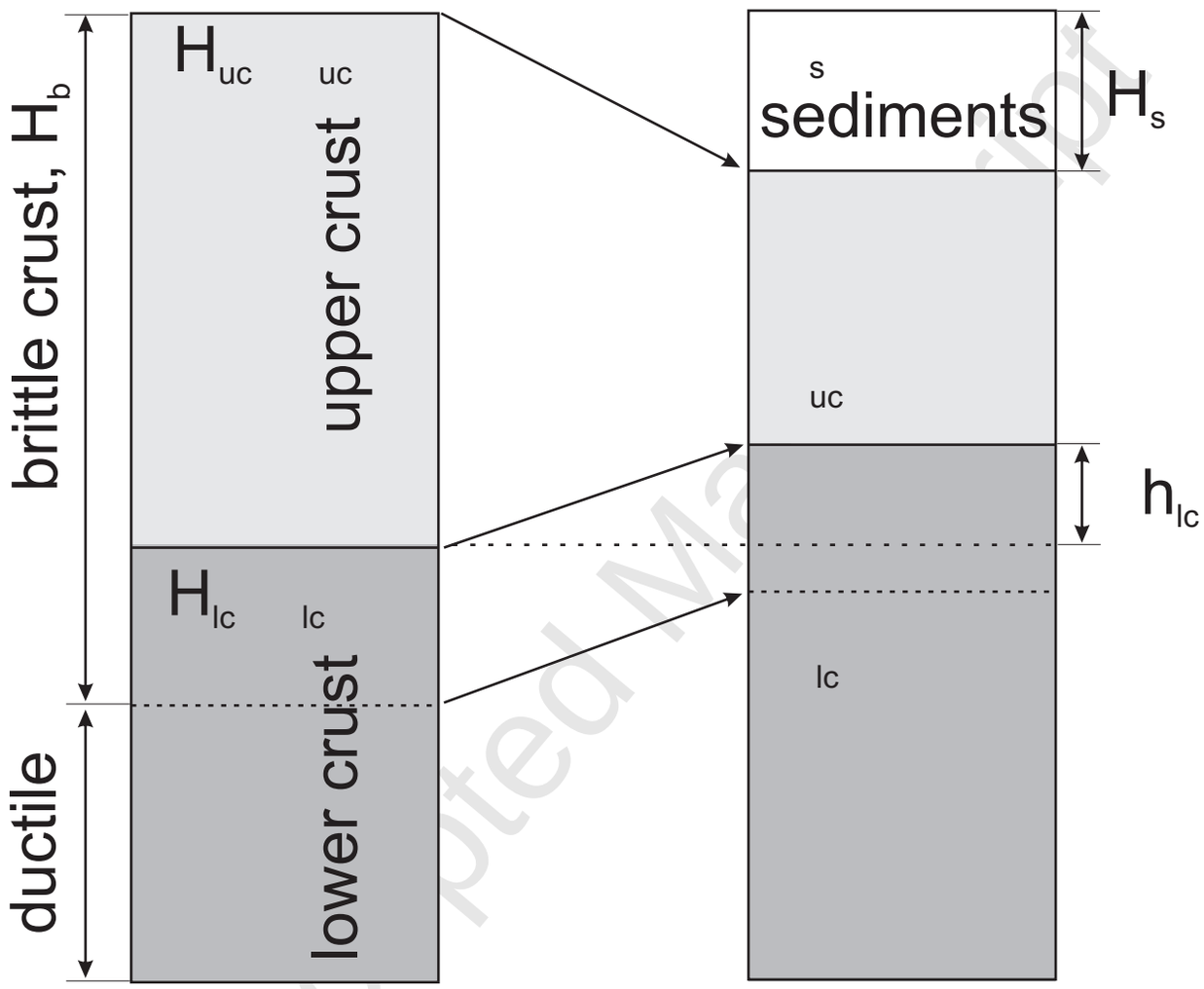

Fig.13

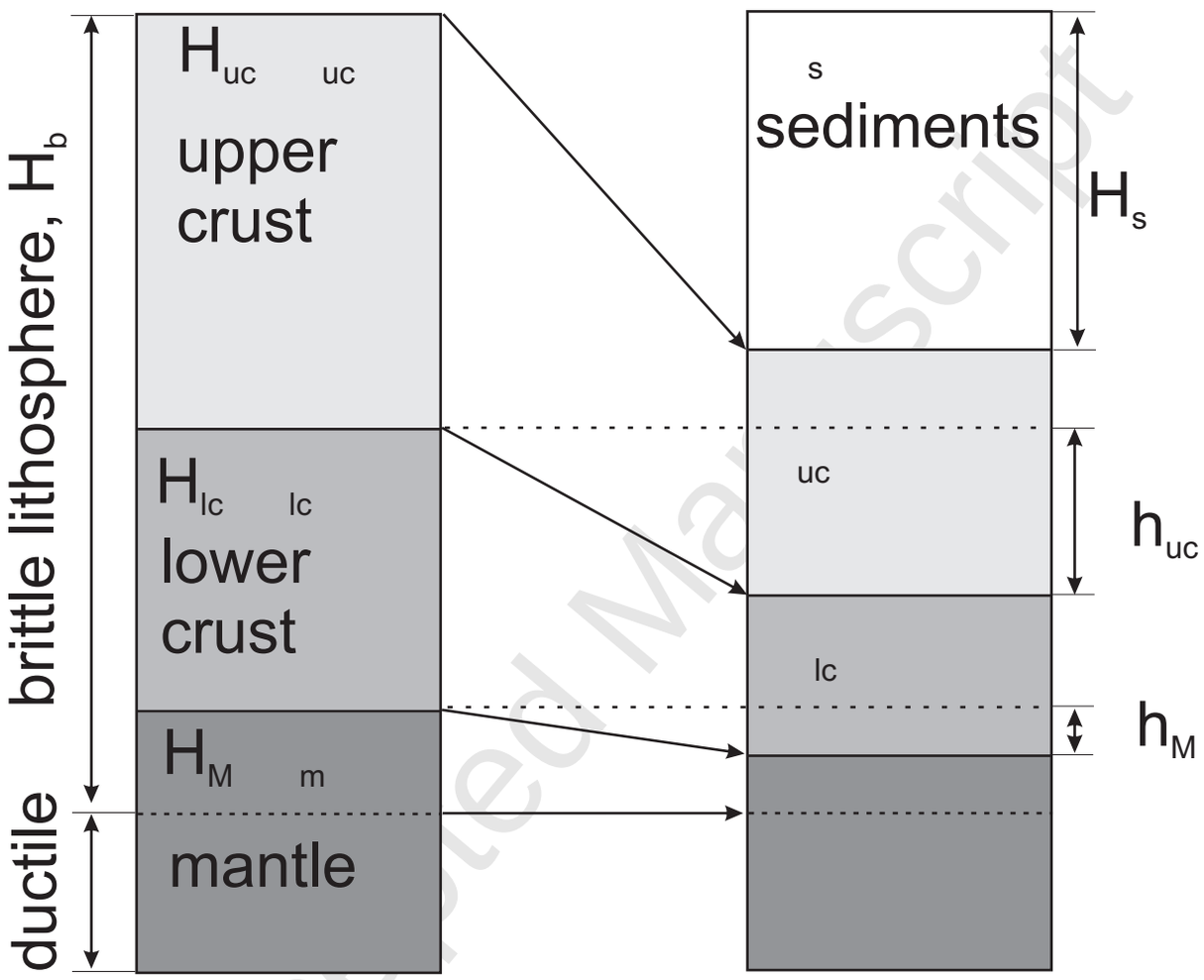

Fig.14

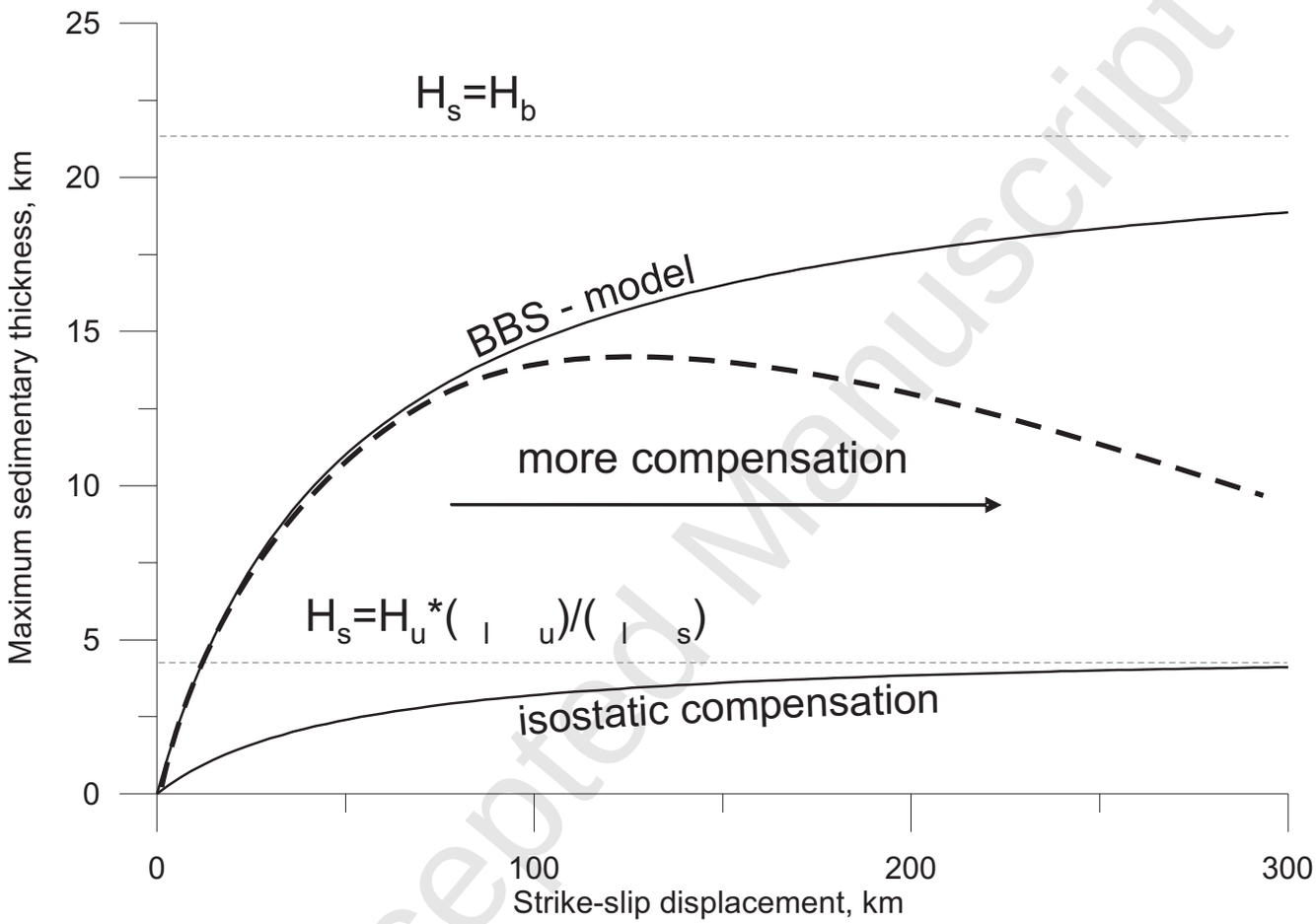

Fig.15

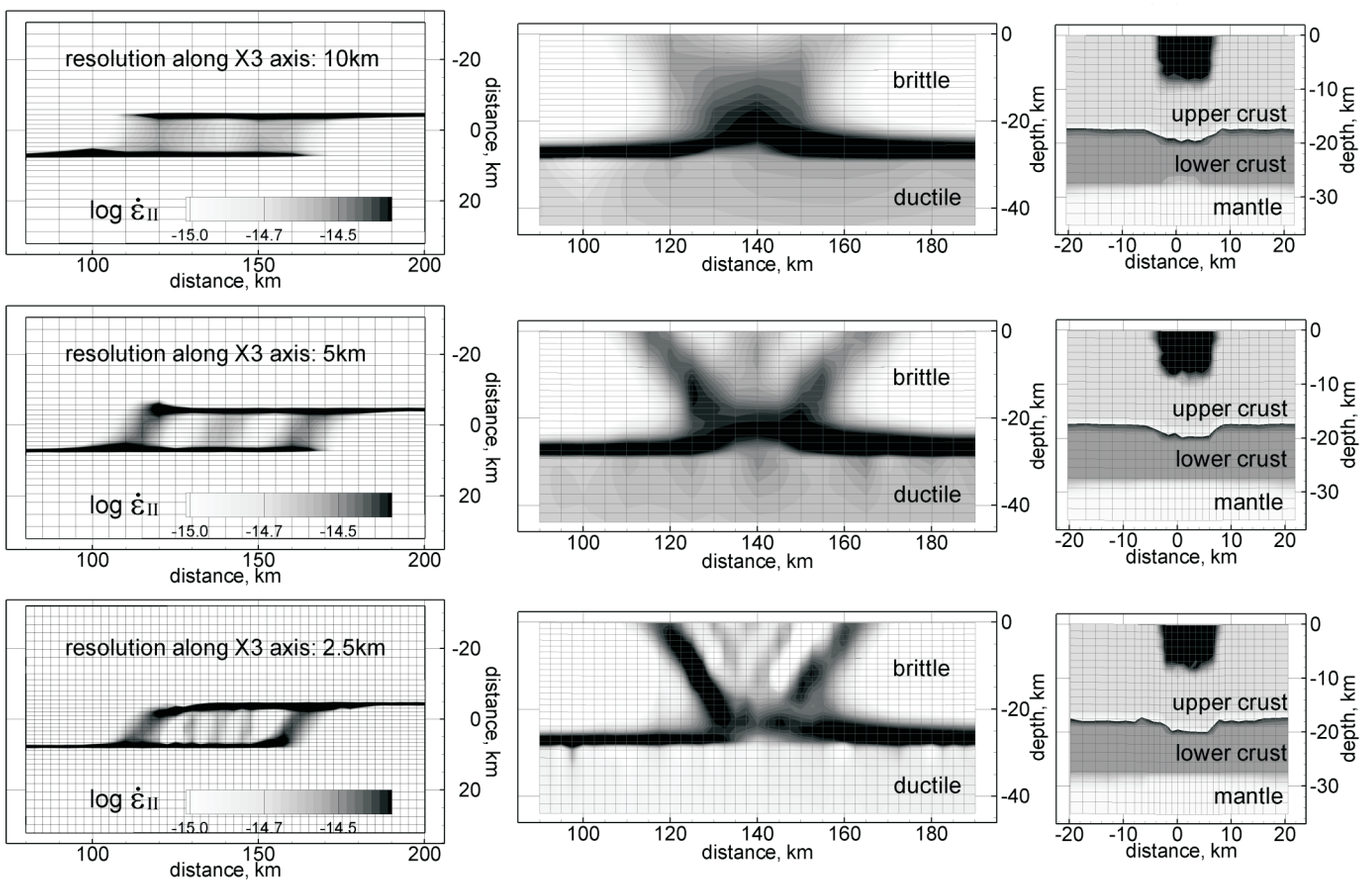

Fig. A1